Periodic Solar Wind Structures Observed in Measurements of Elemental and Ionic Composition in situ at L1

Irena Gershkovich[1], Susan T. Lepri[1], Nicholeen M. Viall[2], Simone Di Matteo[2,3], and Larry Kepko[2]
[1] The University of Michigan, Ann Arbor, MI 48109, USA; igershko@umich.edu
[2] NASA—Goddard Space Flight Center, Greenbelt, MD 20771, USA
[3] The Catholic University of America, Washington, DC 20664, USA

Abstract

Mesoscale periodic structures observed in solar wind plasma serve as an important diagnostic tool for constraining the processes that govern the formation of the solar wind. These structures have been observed in situ and in remote data as fluctuations in proton and electron density. However, only two events of this type have been reported regarding the elemental and ionic composition. Composition measurements are especially important in gaining an understanding of the origin of the solar wind as the composition is frozen into the plasma at the Sun and does not evolve as it advects through the heliosphere. Here, we present the analysis of four events containing mesoscale periodic solar wind structure during which the Iron and Magnesium number density data, measured by the Solar Wind Ion Composition Spectrometer (SWICS) on board the Advanced Composition Explorer spacecraft, are validated at statistically significant count levels. We use a spectral analysis method specifically designed to extract periodic signals from astrophysical time series and apply it to the SWICS 12 minute native resolution data set. We find variations in the relative abundance of elements with low first ionization potential, mass dependencies, and charge state during time intervals in which mesoscale periodic structures are observed. These variations are linked to temporal or spatial variations in solar source regions and put constraints on the solar wind formation mechanisms that produce them. Techniques presented here are relevant for future, higher-resolution studies of data from new instruments such as Solar Orbiter's Heavy Ion Sensor.

1. Introduction

The Sun's extremely hot (>1 MK) outer atmosphere, the corona, continuously releases plasma, which expands out to form the heliosphere bubble encompassing the solar system in the vastness of the interstellar medium (ISM). This flow of plasma is the solar wind and is characterized by varying solar wind speed, density, temperature, and ion composition. The varying conditions, or states/types of solar wind, that are observed in the heliosphere by spacecraft can provide clues about the processes that govern the formation of the solar wind and affect its propagation throughout the heliosphere. The solar wind is composed primarily of protons, electrons, and alpha particles but also contains heavier ions in trace amounts (Bame et al. 1975). Processes occurring in different types of regions on the Sun and the solar atmosphere result in different elemental and ion fractionation which is preserved as the plasma advects outward from the Sun at supersonic speeds (Ogilvie et al. 1980) due to the collisionless nature of the solar wind beyond the freeze-in radius ($\sim 1.1{-}4R_s$ depending on the element) (Hundhausen et al. 1968). The solar wind, therefore, provides a unique laboratory in which to investigate the fundamental physics at work in the Sun's atmosphere (Viall & Borovsky 2020). However, despite decades of study, the mechanisms that drive its formation and release are still under investigation and many open questions remain.

Historically, the solar wind has been classified into two main categories: slow wind and fast wind. This categorization was based on in situ measurements of plasma speed and temperature as well as ionic and elemental composition, without direct information regarding the sources from which the solar wind originated. Compared to fast solar wind ($V_{sw} > 500$ km s^{-1}), known to originate from coronal holes, the slow solar wind ($V_{sw} < 500$ km s^{-1}) tends to be denser, hotter, and more variable in its properties. In addition, the slow wind is characterized by higher ionic charge states and stronger enhancements of elements with low first ionization potential (FIP) relative to their photospheric abundances (Geiss et al. 1995; Lepri et al. 2013; Viall & Borovsky 2020). The origin of the slow solar wind is still a major outstanding question in heliophysics, with leading theories indicating it could be released from large closed coronal magnetic loops or open fields at the boundaries of coronal holes near active regions (ARs) and quiet Sun (QS) regions (Viall & Borovsky 2020). The elemental abundances found in the slow solar wind are similar to those remotely observed on large coronal loops and are often enhanced by a factor of 2–5 relative to photospheric levels (Feldman & Widing 2003; Laming 2015; Laming et al. 2019). In contrast, the elemental abundances of the fast solar wind are more photospheric in nature, reflecting their direct release from coronal holes (Geiss et al. 1995; von Steiger et al. 2000; Laming 2015; Stakhiv et al. 2016; Brooks et al. 2020). As more observations over longer baselines and across spatial and temporal scales revealed more complexity, it became clear that the historical categorization of slow and fast wind is an oversimplification (Zurbuchen et al. 2002; Stakhiv et al. 2015; Roberts et al. 2020; Viall & Borovsky 2020). However, the variations observed in distinct parcels of solar wind can be related to different source regions, acceleration, and release mechanisms and processes back at the Sun.

The solar wind charge states, or ionic composition, used interchangeably throughout this work, are determined in the low corona where ionization and recombination processes occur and reflect the electron temperature and ion and electron densities in the local environment. Once the plasma has expanded out far enough that the interaction cross sections become too low to influence the plasma, the charge states of individual ions freeze-in, and remain unchanged as they flow out into the heliosphere in the solar wind (Gloeckler et al. 2003; Landi et al. 2012; Gilly & Cranmer 2020). The oxygen (O) charge-state ratio O^{7+}/O^{6+} and the carbon (C) charge-state ratio C^{6+}/C^{4+} can be used as a proxy for coronal electron temperature to provide insight into the sources of the wind (Gloeckler et al. 2003; Landi et al. 2012; Stakhiv et al. 2015).

Elemental abundances of solar wind ions are influenced by fractionation before they flow out into the heliosphere. The FIP effect, which fractionates ions based on their FIP, is determined in the chromosphere, where neutral atoms exist and are differentially ionized and accelerated upward by electro-magnetic forces depending on their FIP (Laming 2015; Laming et al. 2019). Low-FIP elements, such as magnesium (Mg) and iron (Fe), with an FIP of 10 eV or lower, are measured to be enhanced relative to higher FIP elements such as O in the corona (compared to their photospheric values) and are also used to discriminate between solar wind source regions. The FIP effect is substantially more pronounced in some solar source regions than others, as we describe below.

In this work, we identify and examine periodic density structures in the solar wind, observed in heavy-ion signatures, with the intent of studying the origin and processes that release the slow solar wind into the heliosphere. In Section 2, we provide a review of periodic structures previously observed in the solar wind and discuss how we greatly expand upon all past reports of in situ heavy-ion composition variations measured in the solar wind. In Section 3, we describe the methodology that we use to validate data, select events, and identify periodic enhancements using a spectral analysis method specifically designed for extracting periodic signals from astrophysical time series. We focus on high time resolution (12 minutes) composition data from the Solar Wind Ion Composition Spectrometer (SWICS) on board the Advanced Composition Explorer (ACE), which enables us to examine finer spatial and temporal structures. In Section 4, we present four events during which periodic variations of heavy-ion abundances and charge states were observed in situ. We focus on one event as a detailed case study and then examine the results of all four events, taken together, in order to compare and contrast their defining properties. In Section 5, we discuss the meaning of our results and how the events examined in this paper exhibit behavior that does not neatly fit into the historical bimodal solar wind classification, but instead exhibit more subtlety. Finally, in Section 6, we summarize our work and the implications of our findings. The variations in the solar wind composition that are exhibited in all events were formed in the solar atmosphere as the composition cannot evolve en route to Lagrange point 1 (L1). The differences observed between events highlight the complex nature of the formation processes involved. We draw upon previous research to show that the results are consistent with interchange reconnection being the process responsible for the formation of these structures. We suggest that future work focus on conducting larger statistical studies of the ACE/SWICS data set and also applying the techniques given here to

new data sets from higher-resolution instruments such as Solar Orbiter's Heavy Ion Sensor (HIS).

2. Mesoscale Periodic Structures in the Solar Wind

Decades of in situ observations have revealed that the solar wind is not laminar, but rather highly structured at many different scales (Verscharen et al. 2019; Viall et al. 2021). On mesoscales, scales that are smaller than the largest structures in the solar wind but larger than kinetic scales, some structures enter the solar wind directly from the solar atmosphere during their formation while others evolve during propagation. The structures that originate in the solar atmosphere and survive to their detection can retain signatures of the processes that form the solar wind. Mesoscale structures in the solar wind not only provide information about the formation of the solar wind in general, but are also important because they can drive the dynamics of magnetospheres (Di Matteo et al. 2022) and they form the medium through which larger space weather events propagate. Viall et al. (2021) provide a comprehensive review of mesoscales, including periodic density structures, observed throughout the heliosphere. They have been observed at scales as small as several minutes (or ~ 100 Mm) and as large as several hours (or several thousand megameters). References are many, but include measurements in situ in and around L1, in situ in Helios data, as well as remotely in STEREO COR2 and STEREO HI1 data (Kepko et al. 2002; Kepko & Spence 2003; Viall et al. 2008, 2009a, 2010; Viall & Vourlidas 2015; Kepko et al. 2016, 2020; Di Matteo et al. 2019; Kepko & Viall 2019).

Periodic mesoscale structures in proton density at L1 have been studied statistically and shown to preferentially exhibit characteristic frequencies, ruling out turbulence as the formation mechanism (Viall et al. 2008; Kepko et al. 2020). Similar structures in electron density have also been verified to originate directly from the corona by comparison of the in situ observations to periodic structures seen in white light images (Viall et al. 2010; Viall & Vourlidas 2015). Periodic mesoscale structures in alpha and proton densities and the alpha-to-proton ratio have been shown to exist by Viall et al. (2009a). However, only one periodic structure event has been reported using the elemental composition of the solar wind in the ACE/SWICS data (Kepko et al. 2016). Here, we expand on previous studies and explore four such events, looking at variations in elemental composition and charge state, using the 12 minute high-resolution SWICS data set, to explore how the structures could have formed. We test whether these events originate in the Sun by examining trends and structure in this elemental composition and charge-state variations. Our purpose is to identify periodic mesoscale structures for which we have composition data of sufficient quality (adequate counts) and quantity such that we can determine that the periodic mesoscale structures were formed in (or in other words, their source is in) the solar atmosphere. We then link these to general regions and formation mechanisms on the Sun.

3. Methodology

3.1. Spectral Analysis Tools

We use a spectral analysis method (Di Matteo et al. 2021) specifically aimed at extracting periodic fluctuations from physical time series characterized by a red-colored power spectral density (PSD)—for which power decreases as

frequency increases. We give a high-level overview of the relevant aspects here. The method employs the adaptive multitaper technique (Thomson 1982) to evaluate the PSD of the time series and provides different options for determining the background PSD. We do this in order to reliably extract statistically significant enhancements in the spectral power at discrete frequencies and call this the *amplitude* test as it is used to detect enhancements in the spectrum of a certain amplitude above the background fit. Additionally, the method provides a harmonic F-test, which is a statistical test highly responsive to monochromatic and phase-coherent components in the time series, based on a complex-valued regression technique used to characterize signal phase and amplitude (Thomson 1982; Di Matteo et al. 2021).

When possible, we use a combination of both the amplitude and harmonic F-test (in support of the amplitude test) to extract and verify periodic structures in the ACE/SWICS 12 minute data. While both the amplitude and the F-test produce false positives, signals that are identified by both tests independently are unlikely to be false and are associated with true physical signals (Mann & Lees 1996; Protassov et al. 2002; Vaughan 2010; Di Matteo et al. 2021). In the analysis described here, we require all signals to pass at minimum the amplitude test at a 90% confidence level, thus expecting a false-positive rate of 10%. This is a standard confidence threshold, extensively tested with Monte Carlo simulations (Di Matteo et al. 2021), that balances the trade-offs between the potential of false positives and the possibility of missing a physical signal. We put more emphasis on the results of the amplitude test because it extracts signals with a distinct amount of power above the red-colored background PSD of astrophysical time series (Inglis et al. 2015), which is not assured by the F-test alone. For this analysis, we smooth the raw spectra with logarithmically spaced bins in order to provide a smoothed estimate of the spectral background (Papadakis & Lawrence 1993; Di Matteo et al. 2021). We then fit the smoothed spectra to a bending power law. Finally, the significance of any enhancements is evaluated relative to the power (amplitude test) and for phase coherence (harmonic F-test). The modular, highly adaptable IDL implementation of this method, described in this subsection, is freely available (Di Matteo et al. 2020) and is used to analyze each 24 hr segment in the study after they have been prepared and validated as described below.

3.2. Time Series Data: Preparation for Spectral Analysis

Each of the four events nominally spans a total of 72 hr and is divided into three 24 hr windows. In practice, some of the windows that we run spectral analysis on were shorter due to the amount of continuous heavy-ion data that we were able to validate. However, we do examine and show the full 24 hr windows when describing general trends in solar wind properties and composition. The middle 24 hr window of each event satisfies the requirement of having significant counts and continuity in the heavy-ion data. The 24 hr periods before and after are examined in order to provide context about the surrounding solar wind. Each consecutive 24 hr window in each of the four 72 hr events is independently examined for periodicity. Section 3.4 provides further information about what defines an event.

Prior to running the spectral analysis procedure described in the previous subsection, the 24 hr long time series data are first prepared by validation, de-spiking, and resampling routines in order to account for any data gaps, uneven sampling, and outliers. This is necessary for all spectral analysis; it would violate the assumptions of spectral analysis if the data are not resampled to a common time step. The validation step, the criteria for which are specified in this subsection, ensures that there is continuity and counts adequate for running spectral analysis on a given window. We choose a 24 hr period to analyze as this provides us with enough data points (120 points) to run spectral analysis with sufficient spectral resolution. The data are de-spiked by removing outliers that exceed a 5σ threshold above a rolling window averaged version of the time series using 12 data points. The data are then resampled to a 12 minute time step and split into windows that are between 18 and 24 hr long, depending on the quality and continuity of the heavy-ion number density data, which are limited by low counts at this time resolution. In this data set, the other elements typically have much higher accumulated counts over the 12 minute native sampling period of the SWICS instrument.

The percentage of missing data points must be less than a threshold value of 20% for each 24 hr window. The number of allowed consecutive missing data points must be less than a threshold value of 3. Additionally, we require visual inspection to ensure that the time series do not exhibit unexpected features that could interfere with spectral analysis beyond the criteria we have explicitly stated. In Section 4, we give an example of the Fe data validation for an event4.1. We perform this validation for each element and for all 24 hr windows that we analyze.

3.3. Instrument Description and Limitations

The ACE spacecraft orbits around L1; on board is the SWICS instrument, which is a plasma spectrometer designed for measuring heavy ions identical to the SWICS spectrometer flown on the Ulysses mission (Gloeckler et al. 1992, 1998). The SWICS instrument is a triple coincidence time-of-flight mass spectrometer that employs an electrostatic analyzer (ESA) at its entrance to select ions with specific energy-per-charge along with a time-of-flight telescope with integrated microchannel plates and solid-state detectors. The time-of-flight telescope, paired with the ESA, enables measurements of both the ion's energy and time-of-flight for the explicit calculation of its mass, charge, and speed, providing the most robust measurement possible within the instrument's resolution limits. The ACE/SWICS data has been used extensively and the instrument, as well as the data processing techniques, have been described in detail (Gloeckler et al. 1992, 1998; von Steiger et al. 2000; Shearer et al. 2014). While most prior studies with ACE/SWICS have focused on data summed to a 2 hr time resolution, here we use the native 12 minute time resolution data in order to study smaller structures in the solar wind (as was done by Kepko et al. 2016). Since this pushes the statistical limits for some less abundant ions such as Fe and Mg, we rely on the statistical uncertainties in the count rates to limit our selection to intervals with sufficient counts. In Section 4.1, we discuss the validation of the Fe data in detail in order to demonstrate the techniques used to validate all elements that we consider in this work. ACE/SWICS has operated continuously since 1998.

3.4. Event Definition Criteria

Apart from the data validation criteria stated above, we require that each event satisfy the following:

1. The 3 day window does not contain an interplanetary coronal mass ejection (ICME). This was confirmed by using the Richardson & Cane ICME list (Richardson & Cane 2010).
2. At least two elemental composition ratios (out of He/O, C/O, Mg/O, and Fe/O) can be validated, according to the criteria stated above, on the central 24 hr window of the 72 hr total event.
3. At least one elemental composition ratio (out of He/O, C/O, Mg/O, and Fe/O) contains a statistically significant periodic structure, as determined by the spectral analysis methodology described above, during one of the three 24 hr windows comprising the event.

Again, our aim is to identify periodic mesoscale structures for which we have composition data of sufficient quality and quantity so that we can determine that the periodic mesoscale structures were formed in (or in other words, their source is in) the solar atmosphere. A periodic variation in either elemental composition and/or ionic charge state indicates that the periodic mesoscale structures were formed in the solar atmosphere, and not formed en route as the solar wind advects. Comparing and contrasting the spectral analysis results for high-FIP (He/O), intermediate-FIP (C/O), and low-FIP (Mg/O and Fe/O) elemental composition ratios, as well as examining charge-state ratios, allows us to put constraints on the solar atmospheric processes that led to the formation of these structures.

4. Results

4.1. Event Study

We begin by showing an event covering the central 24 hr period on 2002 March 4 (1), which includes validated Fe data. We name the 24 hr period used to initially identify the event the *central* time period, the 24 hr period prior the *beginning* and the 24 hr period after the *ending*. We analyze the beginning and ending segments in order to provide context and show the days before and after the central period, thus characterizing the surrounding solar wind.

Figure 1 shows the plasma diagnostic time series for this event. The gray region, and the dashed black lines, mark the boundaries of the central 24 hr window. From the top to the bottom panel, the time series shown are the 272 eV electron pitch angle distribution function value, proton number density, solar wind bulk speed, solar wind bulk temperature, magnetic field magnitude, and vector components of the magnetic field in the Radial Tangential Normal spacecraft-centered coordinate system (radial in blue, normal in green, and tangential in orange). This event takes place within a stream interaction region (SIR): the increase in the proton density (panel (a)), the positive gradient in solar wind speed throughout the gray central period (panel (b)), and the increase in the magnetic field magnitude (panel (d)) are characteristic of a faster wind overtaking slower wind and the creation of a compression region at the interface (Richardson 2018). The 272 eV electron pitch angle distribution measured by the ACE SWEPAM instrument for this event indicates a heliospheric current sheet (HCS) crossing, evident in the 180° change in the electron pitch angle, beginning at around 2002 March 3 21:00:00.

Figure 2 shows the behavior of the solar wind elemental and ion composition during the 72 hr event. The average elemental abundances observed in fast and slow wind, following Geiss et al. (1995); von Steiger et al. (2000), are overplotted in blue and red, respectively. The typical abundance for C/O is the same for fast and slow winds and is shown in purple for that composition ratio. From the top panel to the bottom, we show the elemental composition ratios Fe/O, Mg/O, C/O, and He/O and the charge-state ratios C^{6+}/C^{4+} and O^{7+}/O^{6+}. We plot the individual components that comprise each ratio in order to show how each element or ion contributes to the variation of the elemental or charge-state ratio that it is a part of. For example, in the central gray region of panel (a), we can see that the Fe and O time series vary similarly, but not identically, during the first half of the segment and then diverge during the second half. This is reflected in the variation of the Fe/O time series by a dip during the latter half of the central segment. The component time series are shown in blue and green and are normalized such that their maximum value corresponds to the maximum value of the overall ratio time series.

The data plotted are validated according to the specifications described in Section 3. The elements that constitute the ratios are composed and validated separately, in order to determine which charge states are to be included, so a validated O data point will not necessarily be validated for Fe. Both elements are required to be validated in order to validate the ratio. Later in this section we show the process and results of validating the Fe data (prior to incorporating it into the Fe/O ratio) for the central segment of this event in order to demonstrate the process used to validate all elemental time series.

Figure 2 shows the relative abundance of low-FIP elements (Mg/O and Fe/O) drop by a factor of 2 over the course of the 72 hr window. The Mg/O ratio in Figure 2(b) drops abruptly at the interface between the beginning and central segments and remains at the 0.1 level during the central and ending segments. Charge-state ratios (panels (e) and (f)) drop by a factor of 5, fairly abruptly, similarly to the Mg/O ratio. The Fe/O ratio in panel (a) drops slowly throughout the central region and then remains at 0.08 during the ending time period. There is a drop in C/O and He/O and a rise in proton density at around 2002 March 3 21:00:00, corresponding to the HCS crossing. Note that this rise in proton density also corresponds to the front edge of the ramp-up in velocity, which is a classic signature of the compression region of a stream interaction.

Figure 3 shows spectral analysis results for the elemental composition and charge-state ratios during the central 24 hr segment of the event. The y-axis shows the power in panels (d)–(f) and (j)–(l) and the F-test value in panels (a)–(c) and (g)–(i). The x-axis shows the frequency in millihertz. The F-test results (panels (a)–(c) and (g)–(i) are marked by red triangles and are shown as peaks rising above the dashed red 90% confidence threshold line. As stated in Section 3, we only consider F-test values that correspond to a concurrent amplitude test result to be valid. Panels (d–f) and (j–l) show the raw PSD (black solid line), the PSD background fit (red solid line), the 90% above background confidence curve (red dashed curve) and the results: purple circle for peaks that pass the amplitude test and black "x" for peaks that pass the amplitude test and the harmonic F-test. Note that all elemental composition ratios with a result exhibit periodic structures at around 0.5–0.6 mHz.
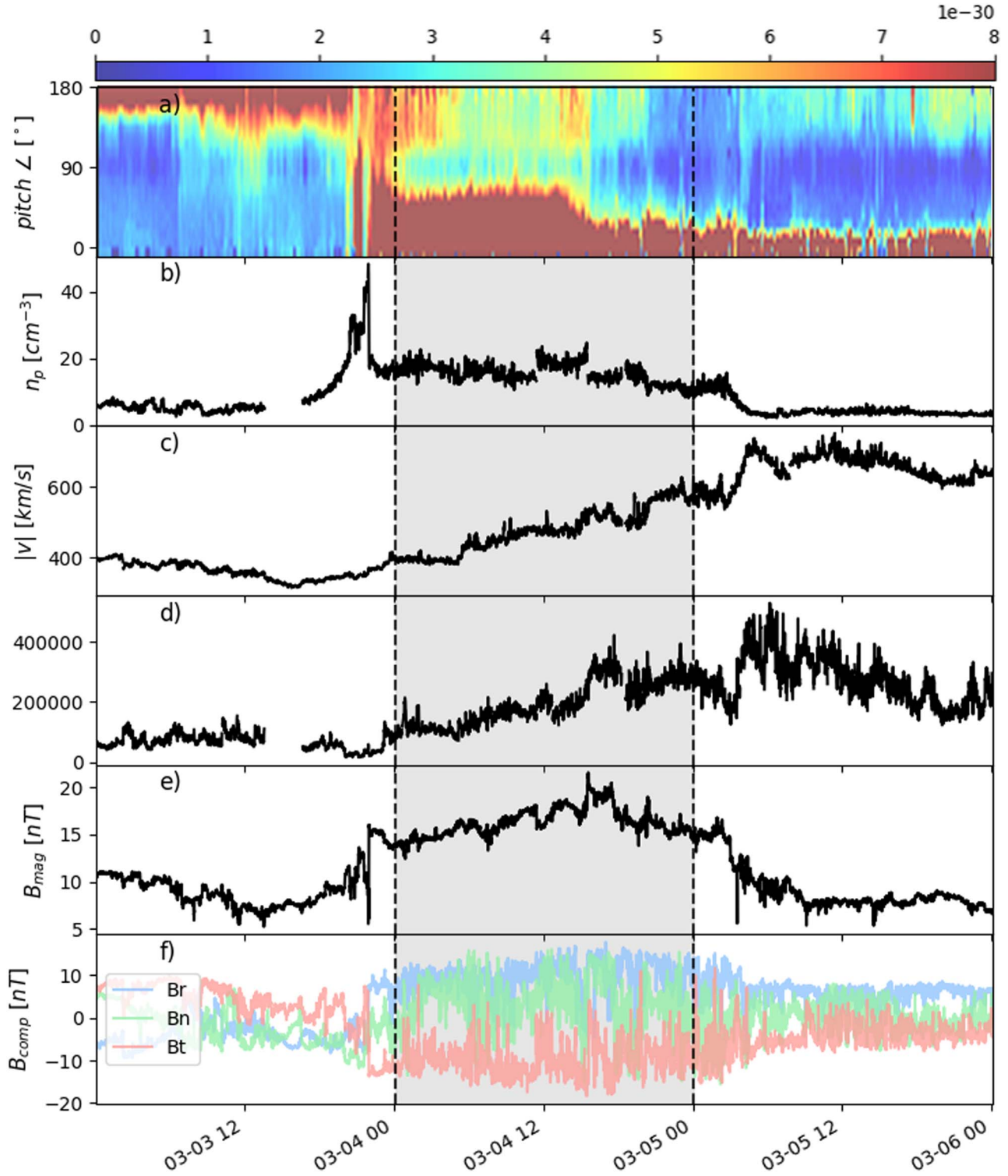
Figure 1. Plasma diagnostic time series plotted for the 2002 March 4 (1) event. The region bracketed by dashed black lines is the central 24 hr segment for the event, selected for its Fe data quality. An HCS crossing occurs just prior to the beginning of the central 24 hr period for this event, as can be seen by the $180°$ change in the 272 eV electron pitch angle distribution of panel (a). Breaks in the time series indicate data gaps in the proton number density and temperature plasma parameters.

Table 1 summarizes the periodic structures associated with this event for each elemental composition (Fe/O, Mg/O, C/O, and He/O) and charge-state (C^{6+}/C^{4+} and O^{7+}/O^{6+}) ratio during the three 24 hr segments. The result columns indicate *low counts* if the counts accumulated by the instrument, per its 12 minute measurement, were insufficient for spectral analysis and "None" if periodic structures were entirely absent from that segment of data. The tests that each selected signal passed are listed in parenthesis after it; "amp" for the amplitude test and "F-test" for the harmonic F-test. Several signals listed in the table pass both tests. Though we identified the event based on the count rates in Fe and the presence of a periodicity in the central 24 hr time window, periodic structures appear throughout the 72 hr event.
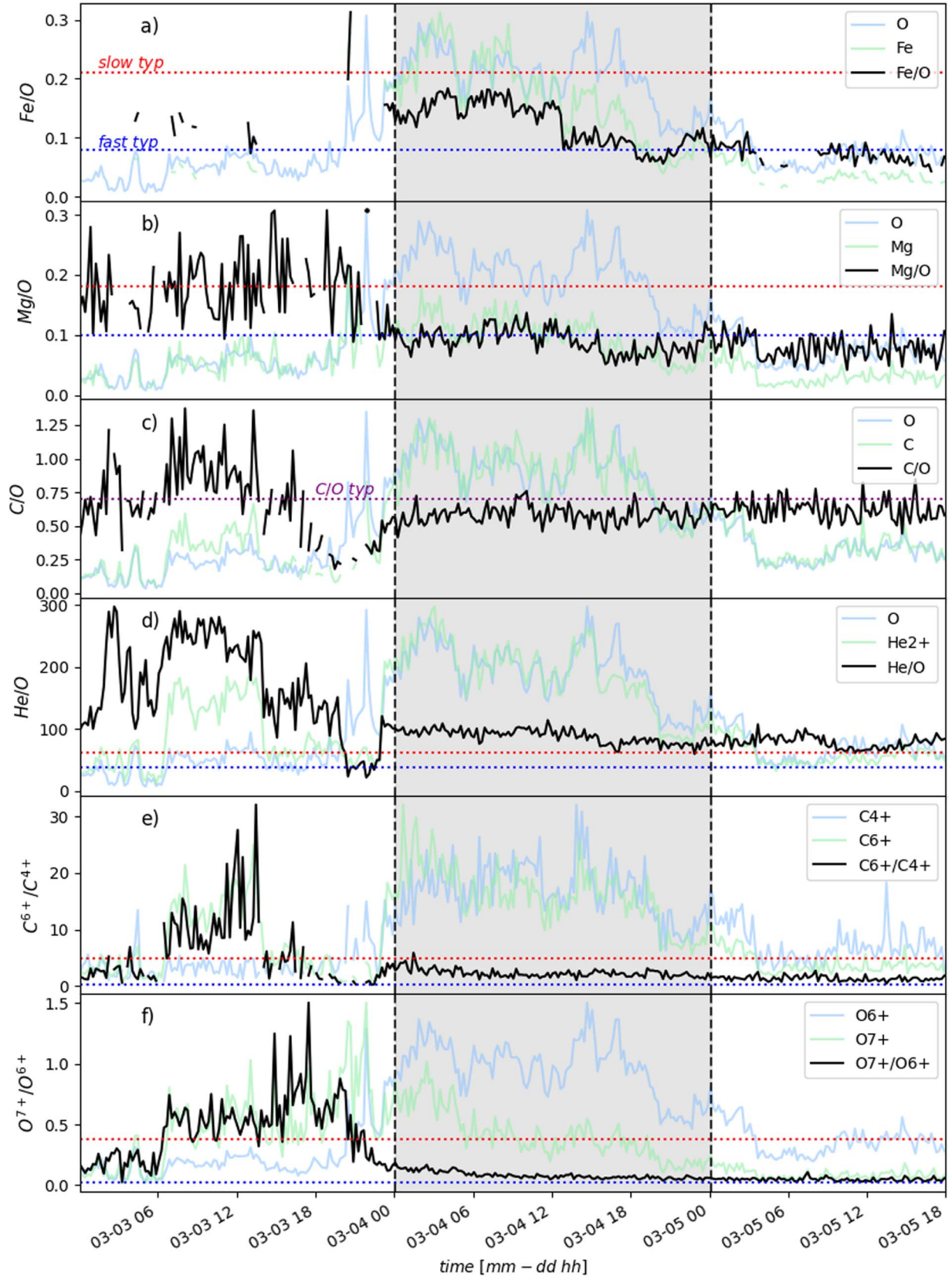
Figure 2. Elemental composition and charge-state ratio time series for the 2002 March 4 (1) event are shown in black. Time series showing the variation of the component elements that comprise each ratio are normalized relative to the maximum of the ratio time series and shown as blue and green traces. The gray region is the central 24 hr segment for the event, selected for its Fe data quality. Breaks in the time series indicate data gaps in the data set. The average fast wind and slow wind abundance values, following (Geiss et al. 1995; von Steiger et al. 2000), are overplotted in blue and red, respectively. The terminology that we use here is a synthesis of terms used in these works. Note that the levels are the same for the C/O abundance, as indicated by the purple line in panel (c).
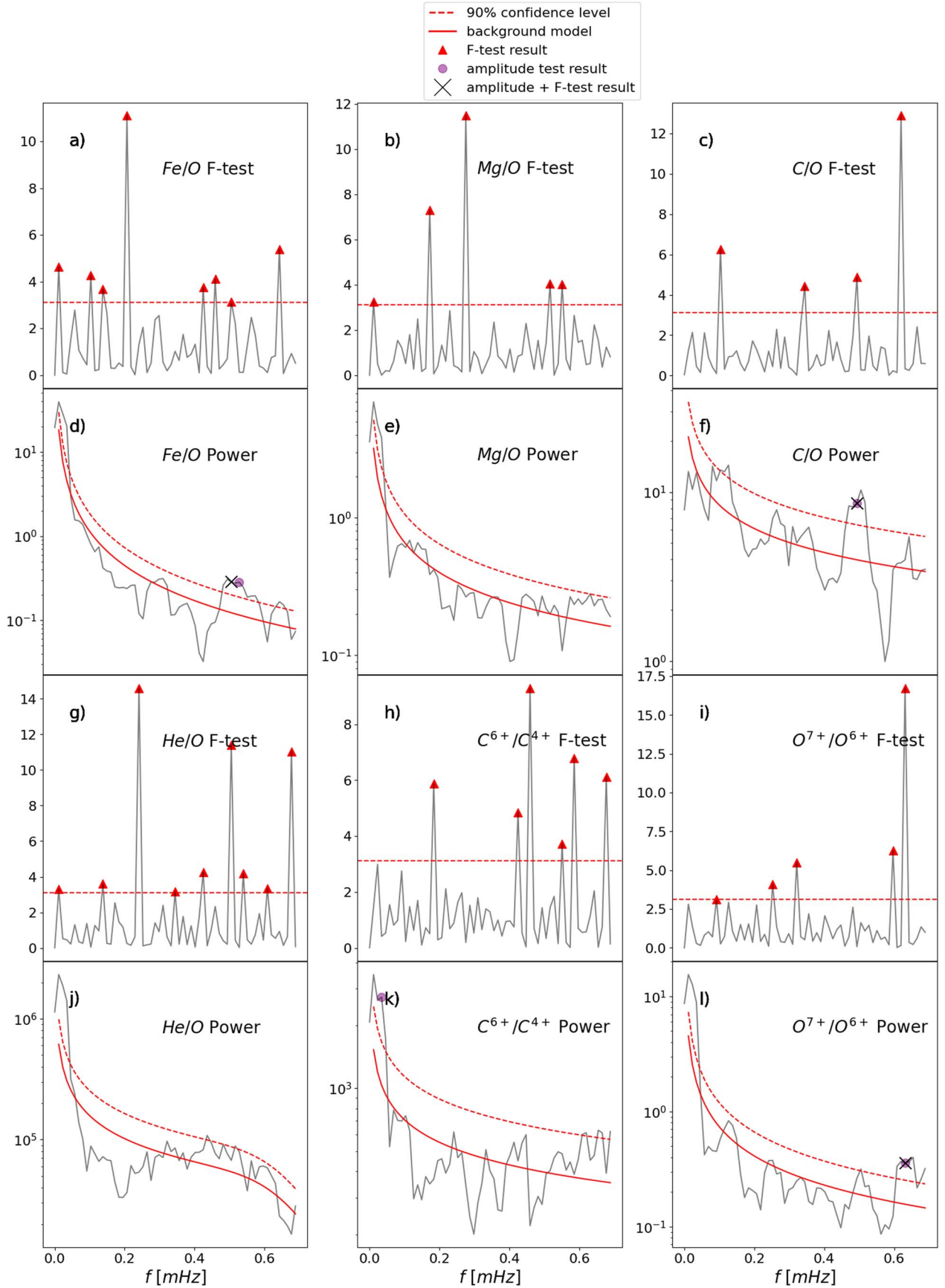
Figure 3. Spectral analysis results for all elemental composition and charge-state ratios. These results correspond to the central time window of the 2002 March 4 (1) event. Panels with the label "F-test" ((a)–(c) and (g)–(i)) show the F-test signals as red triangles, above the dashed red 90% confidence level line. Panels labeled "Power" ((d)–(f) and (j)–(l)) show the estimated power spectral density in gray, the background fit as a solid red line, and the 90% confidence level as a dashed red curve. Results that passed the amplitude test are marked by purple circles. Results that pass both the amplitude and F-test are marked by a black "x".

Table 1
Summary of Periodic Structures Observed in the 2002 March 4 (1) Event

	Beginning	Central	Ending
Fe/O	Low counts	0.51 mHz (amp + F-test)	Low counts
Mg/O	Low counts	None	0.51 mHz (amp + F-test)
C/O	Low counts	0.49 mHz (amp + F-test)	None
He/O	Low counts	None	0.05 mHz, 0.6 mHz (amp)
C^{6+}/C^{4+}	Low counts	0.03 mHz (amp + F-test)	0.37 mHz (amp + F-test)
O^{7+}/O^{6+}	0.64 mHz (amp)	0.64 mHz (amp + F-test)	None

Note. The labels "Low counts" and "None" indicate that the accumulated counts were insufficient for that ratio in that segment or that there were no periodic structures detected with 90% confidence, respectively.

Recall that Fe is the element for which we have the most sparsely validated data, as it is the least abundant. Table 2 shows a manual parameter scan of the different Fe charge states used to validate the ~0.5 mHz peak in the Fe data. The values shown correspond to the central 24 hr segment in this event. This step is performed for all heavy elements, prior to incorporating them into the elemental composition ratios, in order to determine which charge states need to be included for the element. For example, Fe^{10+} is typically the dominant Fe charge state, in terms of abundance and number of counts, but there are others in the data set (see Figure 4). Table 2 is meant to answer the questions: How does missing data in the time series of a given element impact the spectral analysis results? How does adding in data that have been validated at a lower minimum count threshold impact the spectral analysis results? The counts here refer to the number of counts accumulated over the native 12 minute cycle of the SWICS detector, which comprise the data point. Including additional charge states only changes the harmonic F-test result, as shown in the table. Looking across the first to the second and third validation columns, as more charge states are included in the elemental abundance, the ~0.5 mHz peak goes from only passing the amplitude test to passing the F-test as well. This shows that while the details of the spectral analysis for Fe change some as we adjust the validation criteria, the periodicity at approximately ~0.5 mHz is stable and largely insensitive to these adjustments. The Fe panel in Figure 4 shows the charge states that were included in the Fe/O composition ratio after this validation was performed on the Fe data. The Fe element time series is shown as a black dashed line and is validated and incorporated into the Fe/O composition ratio. This figure also shows the construction of all of the elemental time series considered for this event (Mg, C, O He, and Fe). Each charge state is shown in a different color, as indicated in the legend for each panel. The black dotted line in each panel is the sum of the highlighted charge states—the overall element time series. Several charge states tend to dominate the behavior of each element time series and analyses similar to what is presented here for Fe were performed when validating the Mg, O, and C data to ensure that the spectral analysis results were robust.

4.2. Combined Event Analysis

We identified three additional time intervals that met the data validation thresholds and exhibited mesoscale periodic fluctuations of elemental composition and charge-state ratios, namely, 2005 July 27 (2), 2004 January 4 (3), and 2004 February 23 (4). Figure 5 summarizes the periodic structures observed across all time segments and all four events. The black vertical dashed line marks the Nyquist frequency, determined by the SWICS

Table 2
Results of Validating Fe Data for the Central Segment of the 2002 March 4 (1) Event

	50 cts Minimum	16 cts Minimum	0 cts Minimum
Fe^{8+}	0% valid	81% valid	95% valid
Fe^{9+}	65% valid	100% valid	100% valid
Fe^{10+}	89% valid	100% valid	100% valid
Fe^{11+}	77% valid	100% valid	100% valid
Fe^{12+}	53% valid	99% valid	100% valid
Fe^{13+}	0% valid	72% valid	100% valid
Fe^{14+}	0% valid	44% valid	98% valid
Fe amplitude	0.54 mHz	0.53 mHz	0.53 mHz
Fe amplitude + F-test	None	0.51, 0.57 mHz	0.51, 0.56 mHz

Note. The minimum count threshold for the 12 minute data is relaxed allowing more charge states to be included and a larger percentage of the data to be validated (percentage valid). The counts here refer to the number of counts accumulated over the native 12 minute cycle of the SWICS detector. Spectral analysis results match when relaxing validation criteria and including additional charge states. Here, the ~0.5 mHz peak is strongly evident, despite variation in how charge states are combined or the data validation criteria used.

sampling rate. The x-axis shows frequency in millihertz. Significant discrete periodicities are marked with solid circles in colors corresponding to each event, for each 24 hr segment in the event: beginning, central, and ending. Lines representing these segment types are stacked vertically for all elemental and charge-state ratios. The events are labeled by the start date of their central segment and also numbered. The "o" markers on the right side of the dashed line indicate an absence of periodic structure for the segment and the "x" indicates that the segment could not be sufficiently validated due to low instrument counts. The chart shows that there are periodic structures not only during the central 24 hr segment of an event, but often during the 24 hr periods before and after as well.

For some events, the 2002 March 4 (1) event, for example, the dots are aligned vertically, indicating that similar periodic structures were observed for several ratios and/or beginning, central, and ending time segments. The meaning of this will be discussed in the next section. On the other hand, the detected frequencies are sometimes different for different elements and ratios, as the figure also shows. Sometimes the same periodicity persists for several 24 hr segments and sometimes it evolves. The data from each of the four events selected for this study were prepared for spectral analysis and analyzed according to the techniques described in Section 3 and demonstrated in Section 4.1.

In this section, we also show the results of a superposed epoch analysis that we performed in order to compare the evolution of
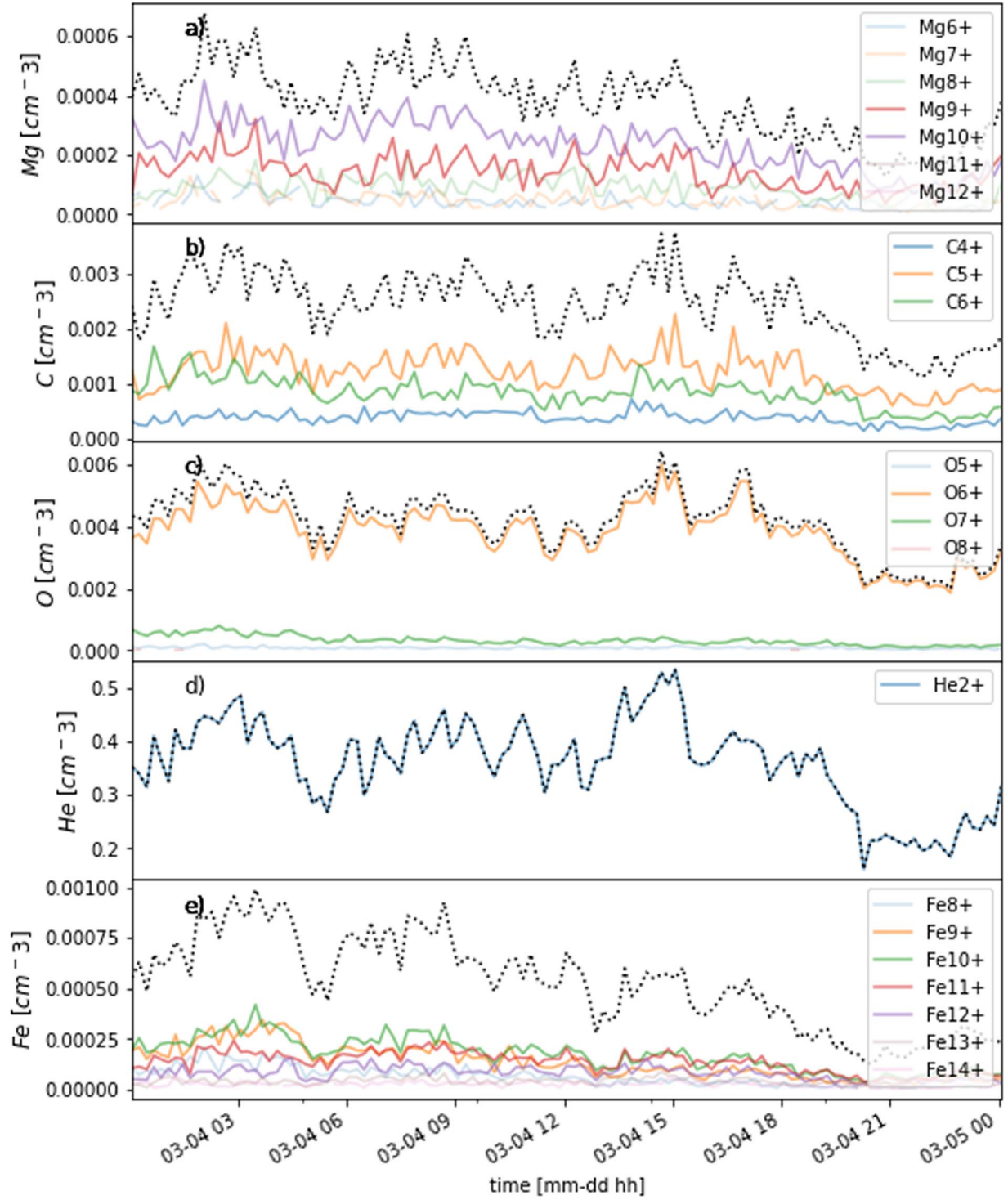
Figure 4. Charge-state selection for the elemental composition ratio data of the 2002 March 4 (1) event. The x-axis shows time, in 3 hr intervals. The y-axis shows the number density per cubic centimeter. Charge-state number density time series that were included in the X/O spectral analysis run is indicated as brighter traces. The dashed line is the sum of the highlighted charge states: the overall X element time series.

the events over longer timescales than the periodicities examined. Specifically, we test whether the elemental composition and charge-state ratios evolve across the 72 hr window analyzed for each event. Figure 6 shows the overall behavior of the charge-state and elemental composition ratios. Since we are focused on the overall trends for this part of the analysis, we used the SWICS 2 hr averaged composition data, for which a high percentage of the data points are validated due to higher

integrated instrument counts. The segments shown here are each 24 hr long and contain the 18–24 hr long segments used in the spectral analysis of the high-resolution data set. Each event is labeled by the start date of the central segment, numbered, and shown in a different color. The 2002 March 4 (1) event examined in the previous subsection is shown here in blue. The fast and slow wind average abundance values, following Geiss et al. (1995) and von Steiger et al. (2000), are overplotted here as
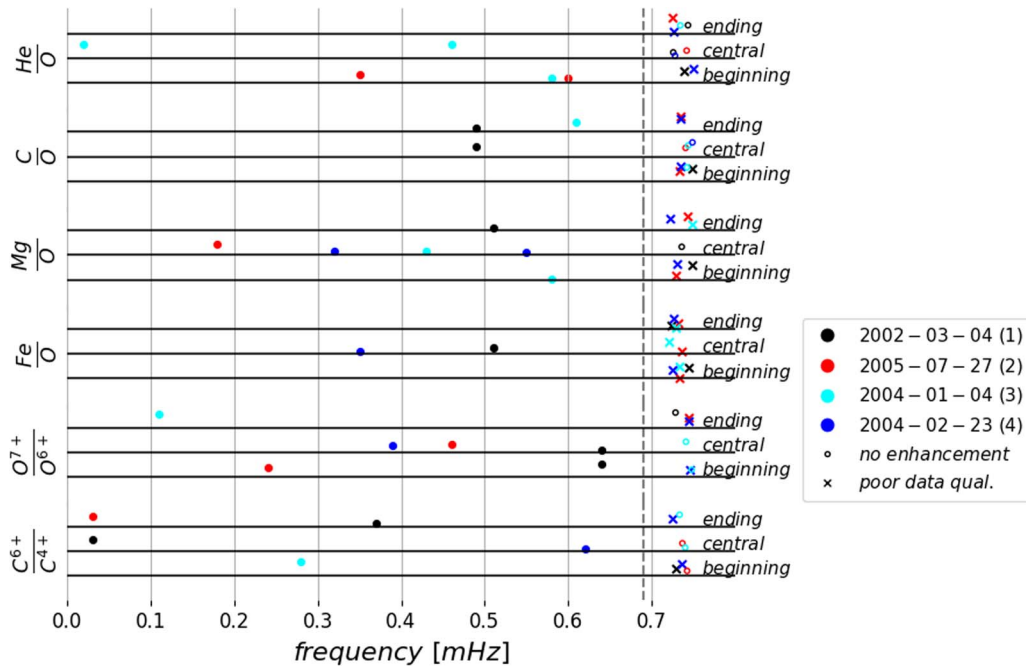
Figure 5. Summary of all periodic structures observed. Beginning, central, and ending 24 hr time segments are shown for each elemental composition and charge-state ratio. We have included an analysis of the 24 hr prior to and after the central window in order to provide context. Each result is shown in a color matching the event that it belongs to. The dashed line marks the Nyquist frequency, which is determined by the SWICS sampling rate. An "o" off to the right of the dashed line indicates that periodic structures were not present in a segment and an "x" indicates that the data could not be validated due to low count rates. Several events, such as the 2002 March 4 (1) event, show multiple ratios with similar periodic structure.

blue and red dotted lines, respectively. The C/O observed abundance levels are the same for the fast and slow solar wind types and this level is indicated by a dotted purple line in panel (b). The mean value of the four event time series is plotted as a dashed black line. The x-axis shows the index of each data point, with zero marking the beginning of the central 24 hr period. The average value of each elemental composition and charge-state ratio, μ, is indicated for each of the three time segments in the plot.

Similar to what we observed in the event study, we see the Mg/O ratio, for event 1 and event 2, drop from close to a typical slow wind to a typical fast wind value. This happens pretty abruptly at the start of the central gray region. The charge-state ratios, O^{7+}/O^{6+} and C^{6+}/C^{4+} in panels (e) and (f), follow a similar trend for these two events. As in the event study, the Fe/O in panel (d) transitions slowly and most of the transition happens in the gray central 24 hr segment. Note that the range spanned by the ratios in the two 2004 events, shown in red and purple, is less than the full fast to slow wind range.

Figure 7 shows the bulk plasma parameters, using the ACE/ SWICS 2 hr resolution data, for the four events: (a) proton density, (b) solar wind speed, (c) proton temperature, and (d) the magnitude of the magnetic field. The x-axis shows time in hours. The gray region marks the central 24 hr period of the events and begins at hour zero. Two of the events, the 2002 March 4 (1) event plotted in blue and the 2005 July 27 (2) event plotted in green, are SIRs with high densities in the compression region. Evidence for the stream interaction can be seen in Figure 7: the sharp rise in the proton density near the start of the gray central period (panel (a)), slow rise in the solar wind speed throughout the central period (panel (b)), and an increase in the magnitude of the magnetic field in the central period of the event (panel (d)). Though our event definition criteria were not for that particular type of wind per se, very

dense wind tends to have high count rates for the heavier elements, which makes it possible for us to validate sparse data such as the Fe and Mg data.

Figure 8 shows the 272 eV electron distribution function by pitch angle for the full 72 hr duration of each event. The events are again labeled by the start date of their central 24 hr segment, are numbered and appear in their own panels. The y-axes in each panel show the pitch angle in degrees and the color bar indicates the magnitude of the distribution function. The x-axis shows time and the central 24 hr segment is bracketed by dashed black lines. The 2002 March 4 (1) event and the 2005 July 27 (2) event coincide with an HCS crossing, as can be seen in Figure 8 where the electron pitch angle changes by 180° for these two events near the start of their central segments. The He/O and C/O time series for these events, plotted in Figure 6 as purple and green traces, show large dips at times corresponding to the HCS crossing. Note that these two events are also SIRs. To summarize, event 2002 March 4 (1) and event 2005 July 27 (2) both exhibited large compositional trends across the 72 hr, were SIRs, and contained HCS crossings. Event 2004 January 4 (3) and event 2004 February 23 (4) had no long-term trends in the changes of composition or speed and were not associated with the HCS.

5. Discussion

We have analyzed and presented here four 72 hr event windows that contain periodic structures in the elemental composition and charge state of the solar wind. These observations greatly expand upon previous work on mesoscale periodic structures in the solar wind; there has only been one other event analyzed using charge states and heavy-ion data (Kepko et al. 2016), which also required the use of the SWICS instrument's 12 minute native resolution in order to observe variations on *mesoscales*. Here, we add four events to this list and incorporate additional elemental composition and charge-
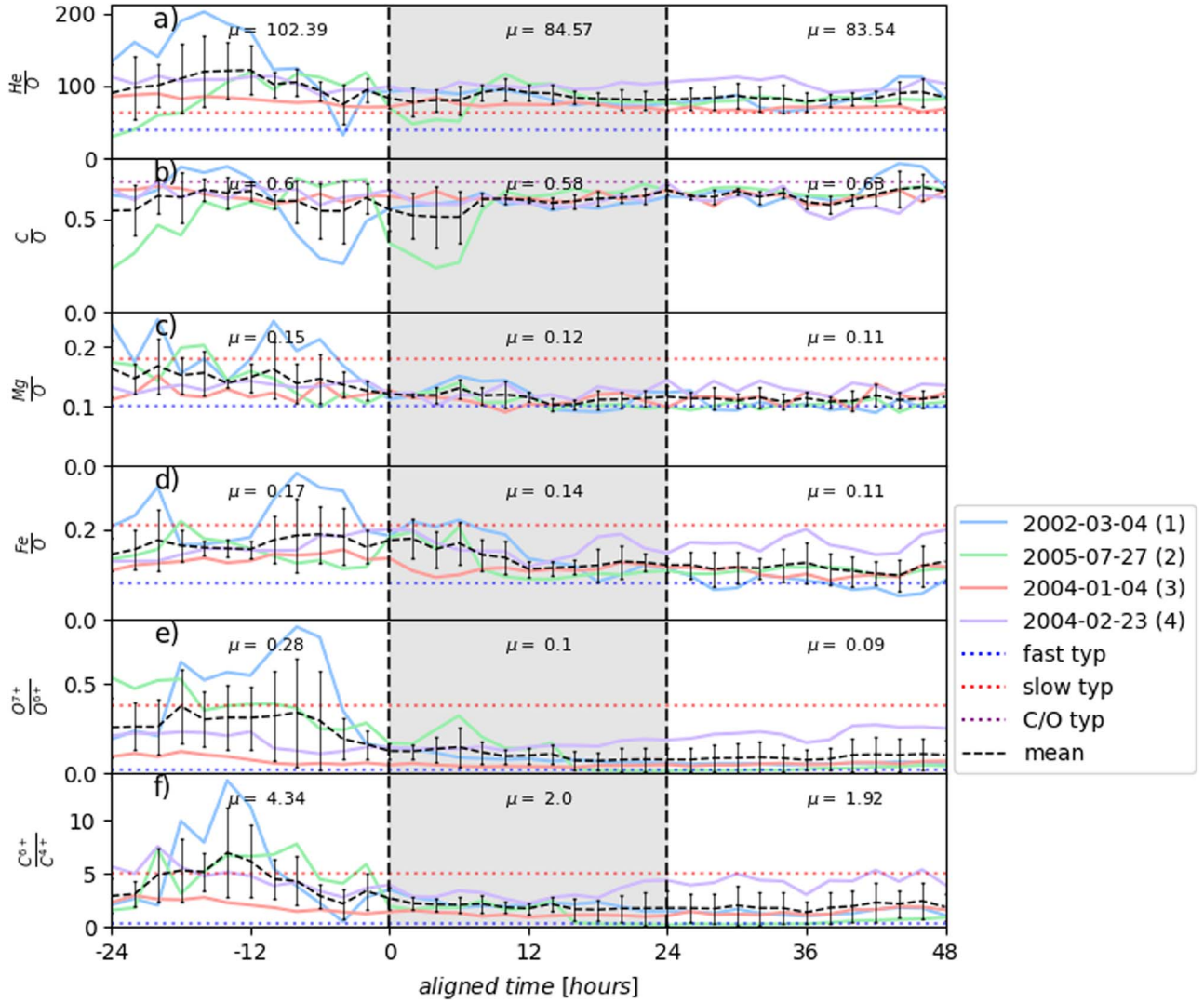
Figure 6. Superposed epoch analysis plots showing the overall evolution of the elemental composition and charge-state ratios throughout each event. The gray segment marks the 24 hr central time window, for which there was the highest rate of validated heavy-ion data, and the white regions before and after show the behavior of each time series in the 24 hr windows preceding and following it, provided for context. The central period begins at hour zero. The *x*-axis shows time, aligned for all events, in hours. The mean value of all events during each 24 hr segment, μ, is computed and marked on the plot.

state ratios into the analysis that go beyond what was available for the event in Kepko et al. (2016). Specifically, by looking at low-FIP elemental composition ratios as well as the O and C charge-state ratios, we have been able to make observations that provide insight into the possible mechanisms underlying the formation of these structures. We also examine high-FIP (He/O) and intermediate-FIP (C/O) ratios in order to compare and contrast.

The limiting factor in this analysis was the low count accumulations that the ACE/SWICS instrument could attain for the Fe and Mg number densities at the 12 minute native sampling rate. These data are particularly important in observing the behavior of the relative abundances of the low-FIP elements across the periodic events. Both the Mg/O and Fe/O composition ratios are low-FIP ratios; thus, monitoring them indicates that if their abundances are elevated the source is likely to be a typical AR or QS region rather than a typical CH type location. Comparing the behavior of these ratios to the behavior of high-FIP elemental composition ratios such as He/O, intermediate-FIP composition ratios such as C/O and charge-state ratios provides information about the likely solar

wind interactions, such as interchange reconnection, occurring at the Sun. Combining charge states, validating and preparing these data for spectral analysis required parameter scans, manual visual inspection, and some judgment calls. The need to perform spectral analysis places a stringent requirement on the data that one can use. We require 24 hr segments of nearly continuous data, since validating a significantly shorter time segment is not sufficient to compute robust spectra with the necessary spectral resolution. The data that could be validated by these means determined event selection and had important implications for the density of the plasma observed.

Two of the events presented here were SIRs, likely because their increased density enabled higher count rates and thus easier to validate Fe and Mg data. Selection criteria aside, these are an interesting class of events to consider as the observed periodicities in elemental composition and charge state capture real information about processes occurring in the Sun. These two events also occurred near an HCS crossing, which is in line with the previous work reporting periodic structure in the C/O ratio occurring near an HCS crossing (Kepko et al. 2016) and consistent with the observation of periodic structures on these
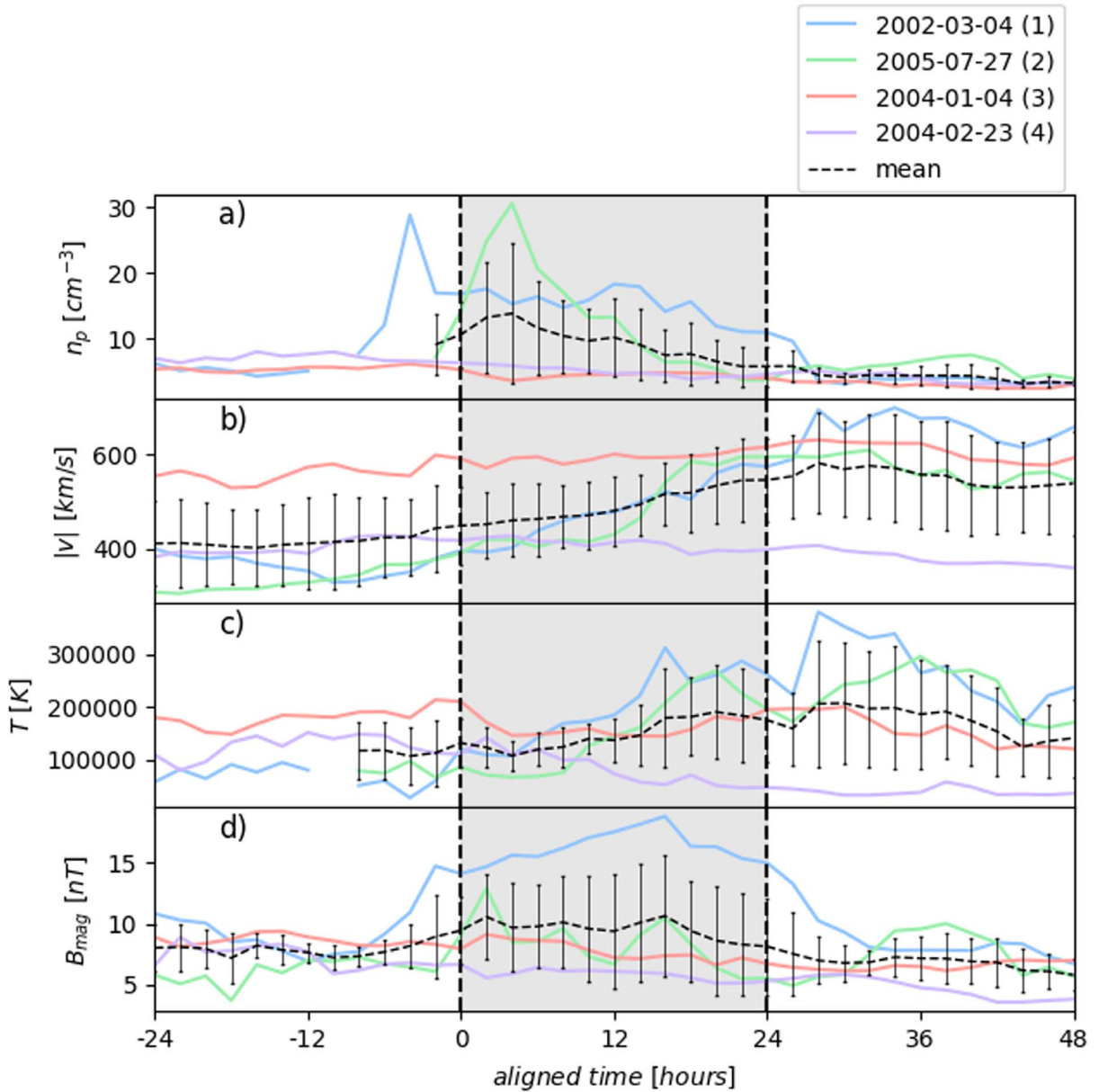
Figure 7. The bulk plasma parameters (a) proton density, (b) solar wind speed, (c) proton temperature, and (d) the magnitude of the magnetic field. The *x*-axis shows time, aligned for all events, in hours. The gray region marks the central 24 hr period of the events and begins at hour zero. The mean for all three events is shown as a black dashed line. Error bars indicating 1σ deviation from the mean are shown. There is missing proton density and proton temperature data for the 2005 July 27 (2) event during the beginning 24 hr segment and the mean and error bars are omitted in that region. The plasma bulk parameter data are obtained from the ACE SWEPAM instrument.

scales observed in and around helmet streamer tips and also associated with the HCS (Viall et al. 2010; Viall & Vourlidas 2015).

The structures found in all four events, observed in situ, are indicators of elemental and ion composition variations being imprinted onto the solar wind from the solar atmosphere. The magnetic field variations during the periods we present here do not exhibit a one-to-one correlation to the variations in elemental composition and charge state. Therefore, we can rule out Kelvin–Helmholtz instability across the stream interface or other boundary wave phenomena (Crooker et al. 1996) as being the underlying mechanism of formation. We performed a superposed epoch analysis in order to determine whether there were commonalities across the 72 hr event studies but found that there were not, aside from the presence

of periodic structures. Nevertheless, plotting the four events together on one plot was a good way to compare and contrast their properties. For the 2002 March 4 (1) and 2005 July 27 (2) events, we see similarities: a slower wind with an enhanced abundance of low-FIP elements and high charge state in the beginning segment is overtaken by a faster wind with less of an enhanced abundance of low-FIP elements and lower charge states. The 2004 January 4 (3) and 2004 February 23 (4) events show fairly steady solar wind speeds, the former being fast and the latter remaining slow throughout the 72 hr event. The 2004 January 4 (3) event exhibits a 3 day trend similar to that of the SIR events, though smaller in amplitude. The 2004 February 23 (4) event does not exhibit a 3 day trend in either direction with regard to the elemental and ion composition. These events highlight the fact that the solar wind types are characterized by
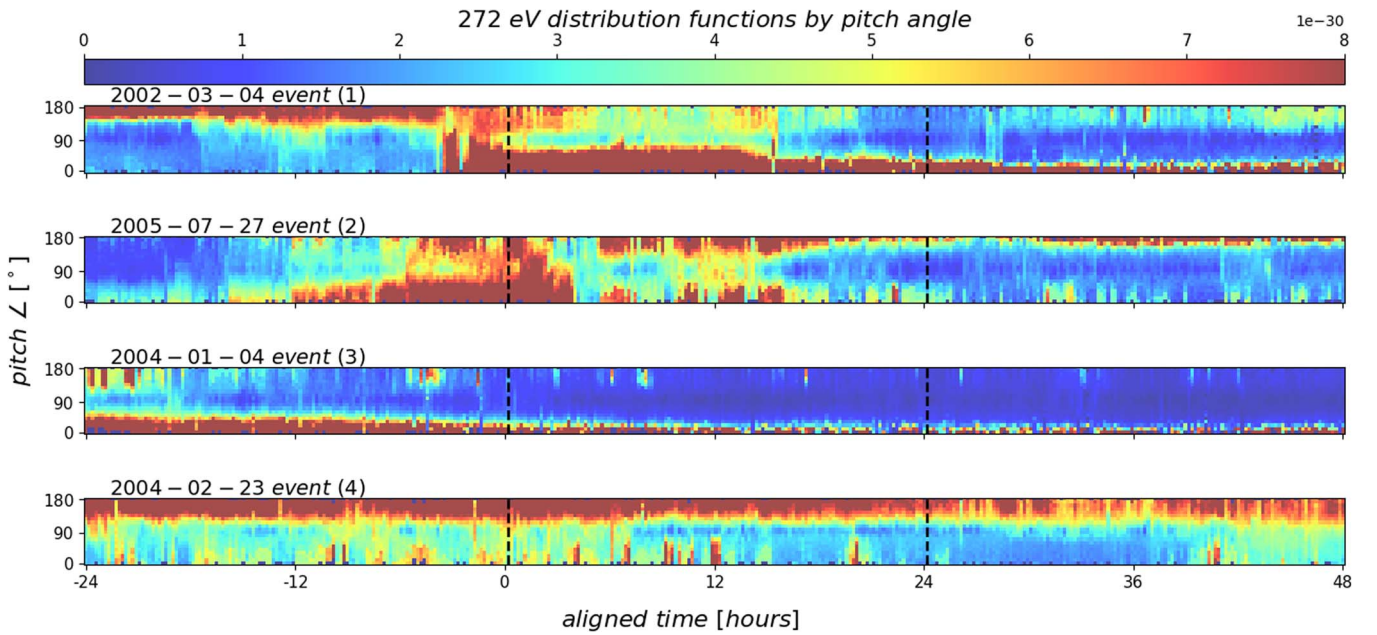
Figure 8. The 272 eV electron pitch angle distributions for each event. The events are labeled by the start date of their central 24 hr segment and numbered. The black dashed lines mark the start and end of the central 24 hr time segment within each event. The aligned time in hours is shown on the *x*-axis and the *y*-axis indicates the pitch angle in degrees. The color bar indicates the value of the electron distribution function for each pitch angle and time. HCS crossings occur near the beginning of the central 24 hr period for the 2002 March 4 (1) and 2005 July 27 (2) events as can be seen in the 180° change in the pitch angle.

a complex combination of their composition signatures as well as their speeds. This has been reported by Zurbuchen et al. (2002) and what we see in these four events is consistent with the report. Solar wind categorization cannot be considered to be strictly binary (Zurbuchen et al. 2002; Stakhiv et al. 2015; Roberts et al. 2020).

As noted earlier, an HCS crossing occurs at the beginning of the central window in two of the events: 2002 March 4 (1) and 2005 July 27 (2). At these times, a drop in the He/O composition ratio is observed. This is in line with He depletions previously reported near the HCS (Borrini et al. 1981; Suess et al. 2009). The behavior of the He/O ratio also exemplifies a wind elemental composition that is complex and nonbinary. The 2002 March 4 (1) event exhibits a high He/O ratio that decreases in the central and ending segments. The other three events do not exhibit strong trends in He across the three days. In all four cases, the abundance is higher than the slow streamer wind levels from Geiss et al. (1995) and von Steiger et al. (2000) for the entire 72 hr duration. Neither of the SIR events (events 1 and 2) follows the speed-He abundance correlation found for long-term averages by Kasper et al. (2007).

We examine the events in the context of what is known about the composition of different types of source regions of the solar atmosphere and how they interact. Interchange reconnection (Crooker et al. 2002; Fisk 2003; Antiochos et al. 2011) between closed magnetic field regions and open magnetic field lines is one possible explanation for how periodic structures enter the solar wind (Viall et al. 2009b; Viall & Vourlidas 2015; Kepko et al. 2016; Higginson & Lynch 2018; Di Matteo et al. 2019; Réville et al. 2020). The S-Web model (Antiochos et al. 2011) predicts that interchange reconnection occurs at the magnetic open-closed boundary, the boundary between closed loops and magnetic field lines open to the heliosphere, which is consistent with what we observe. In the interchange reconnection model, low-FIP enhanced and high charge state enhanced plasma builds up in the closed

magnetic field regions. Additionally, gravitational settling in large closed magnetic field loops may cause heavier ions to be depleted. Gravitational settling makes the observations mass dependent due to heavy ions sinking to the bottom and lighter elements escaping first. An in-depth treatment of this topic can be found in Endeve et al. (2005). If these closed-loop regions periodically reconnect with open field lines, they could create the observed periodic changes in the elemental and ionic composition. Similar observations were reported by Kepko et al. (2016). While there are ideas as to how periodicities could be created at the Sun (Pylaev et al. 2017; Réville et al. 2020), many more events are needed to thoroughly investigate those mechanisms.

Figure 5 shows that several elemental composition and/or charge-state ratios exhibit similar behavior in the frequency domain during a given event. In the 2005 July 27 (2) event, the low-FIP Mg/O ratio and O^{7+}/O^{6+} charge-state ratio exhibit comparable periodicities at approximately 0.2 mHz. The 2004 February 23 (4) event shows similar, though slightly shifted, periodic structures in the Fe/O, Mg/O, and O^{7+}/O^{6+} ratios all occurring within the 0.3–0.4 mHz range. The fact that the low-FIP elemental composition and charge-state ratios behave similarly during these events is consistent with periodic interchange reconnection being the underlying mechanism, occurring at the corona and periodically releasing closed-field plasma into the heliosphere (Kepko et al. 2016; Sanchez-Diaz et al. 2019).

The 2002 March 4 (1) event shows very similar periodic structures in the Fe/O, Mg/O, and C/O composition ratios. The 2004 January 4 (3) event shows comparable structures for the Mg/O, C/O, and He/O ratios. These events feature more complex interactions than do events 2 and 4. We expect the Fe/O and Mg/O ratios to behave similarly as both Fe and Mg are heavy, low-FIP elements.

The behavior of the He/O composition ratio, if governed by the FIP effect only, might be expected to differ from the

behavior of low-FIP ratios such as Mg/O during the 2004 January 4 (3) event. Recall that He is a very high-FIP element. However, He abundances are well known to be only partially explained by the FIP effect, and gravitational settling is likely to be playing a role as well (Laming 2015). He abundances are modulated by the large-scale global coronal magnetic field topology (Moses et al. 2020), including the presence or absence of ARs (Kasper et al. 2007).

The fact that the C/O ratio behaves similarly to the low-FIP ratios in events 1 and 3 may be explained by the fact that C is an intermediate-FIP element with an FIP of just over 10 eV—it follows the behavior of high-FIP elements when fractionation occurs in closed-field loops but can behave like the low-FIP elements if fractionation occurs at the origin of an open-field area (Laming et al. 2019). The in situ solar wind is a mixture of plasma that originates from both closed- and open-field regions and the nature of the mixture depends on the details of the reconnection event. Due to this, the C/O ratio may match the behavior of low-FIP elemental composition ratios as seen in Figure 5 for the 2002 March 4 (1) and 2004 January 4 (3) events. The variation in composition, produced by processes in the solar atmosphere, is the commonality among all four events. The different manifestations of these variations highlight the complex, multistep processes involved in the formation of these mesoscale structures.

6. Conclusion

Four events containing mesoscale periodic structure in the solar wind's elemental and charge-state composition were extracted from the ACE/SWICS 12 minute data set, validated, analyzed, and examined within the context of spectral analysis. The common feature among all four events is the variation in composition. Such variation can only have been produced in the solar atmosphere and therefore provides important constraints on the formation mechanisms responsible. The differences in the variations observed highlight the complexity of the multistep processes involved in the creation of these mesoscale structures.

The events were selected based on the quality of the Mg and Fe number density data, which typically accumulate low counts at the 12 minute ACE/SWICS native resolution, in order to test whether the presence and values of periodicities exhibited FIP or charge-state biases. The results showed that events 2002 March 4 (1) and 2005 July 27 (2) occurred during HCS crossings and were SIRs, with the expected drop in the He/O ratio. The 2004 January 4 (3) event did exhibit the same general trend of decreasing low-FIP abundance and charge state as did the two SIRs and HCS events over the 72 hr period examined, but the 2004 February 23 (4) event did not exhibit much of an overall trend in elemental and ion composition throughout the time span of the event.

The periodic structures observed in these events also captured interesting relationships as described and discussed in Sections 4 and 5 and summarized here. In the 2005 July 27 (2) and 2004 February 23 (4) events, for example, we see one or more low-FIP ratios and a charge-state ratio behave comparably in terms of the periodic signals observed, suggesting that interchange reconnection may be the process responsible for these structures. In the 2002 March 4 (1) event, the low-FIP ratios (Mg/O and Fe/O) contain a similar periodic structure as does C/O. The 2004 January 4 (3) event shows the Mg/O, He/O, and C/O composition ratios containing closely matched

periodic structures. This suggests a more complex interaction for the He/O and C/O ratios than a simple picture where all closed loops have low-FIP enhanced ratios that are constant in time, but these interactions can also be explained by the interchange reconnection model as detailed in Section 5.

We have greatly expanded upon all previous work reported about periodic structures in solar wind elemental and ion composition (Kepko et al. 2016). The techniques presented here can be directly applied to data from new, higher-resolution instruments, such as Solar Orbiter's HIS with its 90 s resolution composition data, in order to extract greater insight into the source mechanisms as well as to determine the spatial and temporal nature of the variation involved. While the event identification in this study was limited by our strict requirement on Mg and Fe count rates, periodic structures in C, O, their charge-state ratios, and He/O appear to be common in the ACE/SWICS 12 minute data set. Future work will be to go beyond these four events and to compute statistics on the periodic mesoscale structures identified in the entire 14 yr ACE/SWICS 12 minute data set.

ORCID iDs

Susan T. Lepri ⓘ https://orcid.org/0000-0003-1611-227X
Nicholeen M. Viall ⓘ https://orcid.org/0000-0003-1692-1704

References

Antiochos, S., Mikić, Z., Titov, V., Lionello, R., & Linker, J. 2011, ApJ, 731, 112
Bame, S., Asbridge, J., Feldman, W., Montgomery, M., & Kearney, P. 1975, SoPh, 43, 463
Borrini, G., Gosling, J., Bame, S., Feldman, W., & Wilcox, J. 1981, JGRA, 86, 4565
Brooks, D. H., Winebarger, A. R., Savage, S., et al. 2020, ApJ, 894, 144
Crooker, N., Burton, M., Siscoe, G., et al. 1996, JGRA, 101, 24331
Crooker, N., Gosling, J., & Kahler, S. 2002, JGRA, 107, SSH 3–1
Di Matteo, S., Viall, N., & Kepko, L. 2020, SPD_MTM: a spectral analysis tool for the SPEDAS framework, Zenodo, doi:10.5281/zenodo.3703168
Di Matteo, S., Viall, N. M., Kepko, L., et al. 2019, JGRA, 124, 837
Di Matteo, S., Viall, N. M., & Kepko, L. 2021, JGRA, 126, e2020JA028748
Di Matteo, S., Villante, U., Viall, N., Kepko, L., & Wallace, S. 2022, JGRA, 127, e2021JA030144
Endeve, E., Lie-Svendsen, Ø., Hansteen, V. H., & Leer, E. 2005, ApJ, 624, 402
Feldman, U., & Widing, K. 2003, SSRv, 107, 665
Fisk, L. 2003, JGRA, 108, 1157
Geiss, J., Gloeckler, G., & von Steiger, R. 1995, SSRv, 72, 49
Gilly, C. R., & Cranmer, S. R. 2020, ApJ, 901, 150
Gloeckler, G., Cain, J., Ipavich, F., et al. 1998, SSRv, 86, 497
Gloeckler, G., Geiss, J., Balsiger, H., et al. 1992, A&AS, 92, 267
Gloeckler, G., Zurbuchen, T. H., & Geiss, J. 2003, JGRA, 108, 1158
Higginson, A. K., & Lynch, B. J. 2018, ApJ, 859, 6
Hundhausen, A., Gilbert, H., & Bame, S. 1968, JGR, 73, 5485
Inglis, A., Ireland, J., & Dominique, M. 2015, ApJ, 798, 108
Kasper, J. C., Stevens, M. L., Lazarus, A. J., Steinberg, J. T., & Ogilvie, K. W. 2007, ApJ, 660, 901
Kepko, L., & Spence, H. E. 2003, JGRA, 108, 1257
Kepko, L., Spence, H. E., & Singer, H. 2002, GeoRL, 29, 1197
Kepko, L., & Viall, N. 2019, JGRA, 124, 7722
Kepko, L., Viall, N., Antiochos, S., et al. 2016, GeoRL, 43, 4089

Kepko, L., Viall, N. M., & Wolfinger, K. 2020, JGRA, 125, e28037
Laming, J. M. 2015, LRSP, 12, 2
Laming, J. M., Vourlidas, A., Korendyke, C., et al. 2019, ApJ, 179, 124
Landi, E., Alexander, R., Gruesbeck, J., et al. 2012, ApJ, 744, 100
Landi, E., Gruesbeck, J., Lepri, S. T., Zurbuchen, T. H., & Fisk, L. 2012, ApJ, 761, 48
Lepri, S., Landi, E., & Zurbuchen, T. 2013, ApJ, 768, 94
Mann, M. E., & Lees, J. M. 1996, ClCh, 33, 409
Moses, J. D., Antonucci, E., Newmark, J., et al. 2020, NatAs, 4, 1134
Ogilvie, K., Bochsler, P., Geiss, J., & Coplan, M. 1980, JGR, 85, 6069
Papadakis, I., & Lawrence, A. 1993, MNRAS, 261, 612
Protassov, R., Van Dyk, D. A., Connors, A., Kashyap, V. L., & Siemiginowska, A. 2002, ApJ, 571, 545
Pylaev, O., Zaqarashvili, T., Brazhenko, A., et al. 2017, A&A, 601, A42
Réville, V., Velli, M., Rouillard, A. P., et al. 2020, ApJ, 895, L20
Richardson, I. G. 2018, LRSP, 15, 1
Richardson, I. G., & Cane, H. V. 2010, SoPh, 264, 189
Roberts, D. A., Karimabadi, H., Sipes, T., Ko, Y.-K., & Lepri, S. 2020, ApJ, 889, 153
Sanchez-Diaz, E., Rouillard, A., Lavraud, B., Kilpua, E., & Davies, J. 2019, ApJ, 882, 51

Shearer, P., von Steiger, R., Raines, J. M., et al. 2014, ApJ, 789, 60
Stakhiv, M., Landi, E., Lepri, S. T., Oran, R., & Zurbuchen, T. H. 2015, ApJ, 801, 100
Stakhiv, M., Lepri, S. T., Landi, E., Tracy, P., & Zurbuchen, T. H. 2016, ApJ, 829, 117
Suess, S., Ko, Y.-K., von Steiger, R., & Moore, R. 2009, JGRA, 114, A04103
Thomson, D. J. 1982, IEEEP, 70, 1055
Vaughan, S. 2010, MNRAS, 402, 307
Verscharen, D., Klein, K. G., & Maruca, B. A. 2019, LRSP, 16, 5
Viall, N. M., & Borovsky, J. E. 2020, JGRA, 125, e26005
Viall, N. M., Deforest, C. E., & Kepko, L. 2021, FrASS, 8, 139
Viall, N. M., Kepko, L., & Spence, H. E. 2008, JGRA, 113, A07101
Viall, N. M., Kepko, L., & Spence, H. E. 2009a, JGRA, 114, A01201
Viall, N. M., Spence, H. E., & Kasper, J. 2009b, GeoRL, 36, L23102
Viall, N. M., Spence, H. E., Vourlidas, A., & Howard, R. 2010, SoPh, 267, 175
Viall, N. M., & Vourlidas, A. 2015, ApJ, 807, 176
von Steiger, R., Schwadron, N., Fisk, L., et al. 2000, JGRA, 105, 27217
Zurbuchen, T., Fisk, L., Gloeckler, G., & von Steiger, R. 2002, GeoRL, 29, 1352